Synchrotron Tomography-Based Finite Element Analysis of Vertebral Endplate Loading Reveals Functional Roles for Architectural Features

Jishizhan Chen[1], Alissa L Parmenter[1,3], Aikta Sharma[1], Elis Newham[2], Eral Bele[1], Sebastian Marussi[3], Andrew A Pitsillides[4], Nick J Terrill[5], Himadri S Gupta[2,*], Peter D Lee[1,3,*]

[1] Mechanical Engineering, University College London, Torrington Place, London WC1E 7JE, UK

[2] School of Engineering and Materials Sciences, Queen Mary University of London, London E1 4NS, UK

[3] Research Complex at Harwell, Rutherford Appleton Laboratory, Oxfordshire OX11 0FA, UK

[4] Department of Veterinary Basic Sciences, Royal Veterinary College, Royal College Street, London NW1 0TU, UK

[5] Diamond Light Source, Didcot OX11 0DE, UK

Correspondence to Himadri S Gupta (h.gupta@qmul.ac.uk) or Peter D Lee (peter.lee@ucl.ac.uk).

Abstract

Lower back pain is linked to vertebral biomechanics, with vertebral endplates (VEPs) playing a key role in vertebral load transfer and distribution. Synchrotron computed tomography (sCT) allows for detailed visualisation of the microstructure of intact VEPs under near-physiological loads and, when coupled with digital volume correlation (DVC), can be used to quantify three-dimensional (3D) strain fields with nanoscale resolution. Herein, we spatially couple DVC data and an image-based finite element model (FEM) to determine the material properties of murine VEPs. This model was then extended to investigate VEP biomechanics under different motions and disease conditions to reveal that VEP protrusions are important for load absorption and redistribution under different motions and predicted that abnormal intervertebral disc (IVD) stress may underpin osteoporosis- and pycnodysostosis-related IVD degeneration. Our study validates the efficacy of using DVC to increase the accuracy of FEM predictions and highlights that these methodologies may be scalable to large animals and humans.

INTRODUCTION

Low back pain is extremely common in all low-to-high income countries and age groups(*1*), and is the leading worldwide cause of disability(*2*), particularly in the aged(*3*). The cause of most low back pain remains unidentified, however, and since physiotherapy and invasive approaches have limited efficacy and significant side-effects, current treatment remains primarily focused on alleviating pain(*4, 5*). Recent evidence has emphasised links between low back pain and intervertebral disc degeneration (IVDD) observed as lesions in the vertebral endplate (VEP)(*6-8*). The VEP has non-uniform structure – thicker in peripheral than central regions(*9, 10*) – that connects cranial-to-caudal vertebrae to the IVD to form interfaces between tissues with differing mechanical properties(*11*). The VEP needs to attain a balance of porosity for solute transport and strong mechanical pressure resistance; a challenge that makes them prone to failure(*6*). To understand the link between structure, tissue properties and failure in VEP, we develop a synchrotron tomography image-based murine lumbar finite element model (FEM) then improve its predictive accuracy using digital volume correlation (DVC) strain. Physiologically relevant complex load transfer systems for robust simulation of second and third principal strains across VEPs were explored to elucidate the biomechanics that may link emergence of VEP lesions to IVDD. Via exploiting a rat model to enhance spatial reliability of stress/strain predictions to elucidate the underlying biomechanics, we demonstrate potential application to humans, with an end goal of speeding development of mechanism-based treatment approaches.

Synchrotron computed tomography (sCT)(*12*) has recently enabled visualisation of intact joint microstructures in static(*13-15*) and under near-physiological loads(*16*). This method allows greater resolution, faster imaging speed, and improved contrast in untreated samples, compared to lab CT. These images also enable the application of DVC to quantify three-dimensional (3D) displacement and strain fields in response to uniaxial compression(*12, 16-19*). This combined sCT/DVC approach is, however, highly labour-intensive and resource consuming, making its routine use unfeasible(*20*). Model based approaches like FEM represent an effective alternative for routine extension of simulations to a range of orthopaedic conditions; however, it relies on the quality of the material property and boundary condition inputs. Lack of accurate inputs for rat spine material properties thus renders development of a method for their calibration critical to an effective FEM and robust predictions of underlying VEP biomechanics.

CT-based DVC coupled with FEM has been used for comparison of FEM predictions with DVC measurements of strain and displacement(*21-24*) and has recently been applied as an inverse method for estimating the Young's modulus of materials, including human isolated single femoral trabeculae(*25*) and fine-grained graphite(*26*). However, these studies have limitations. For instance, the Poisson's ratio was not included in the optimisation, which might cause significant error if there is deviation from reality(*27*). Further, the comparison between FEM predictions and DVC measurements was based on subsamples, lacking accuracy at the level of spatially paired nodes. More importantly, these studies validated only homogeneous and single materials in a simple system. Clinical MRI-based DVC has been used on human IVD's to show strain localisation mechanisms, demonstrating the promise of

upscaling to humans(*28*). Herein, we use the IVD to develop and validate the utility of an inverse method for complex systems containning both soft and hard component parts with sCT-resolved intact microstructures.

RESULTS

Overall Methods

To overcome the previous limitations for understanding the complex VEP biomechanics using modelling, here we develop an automated FEM/DVC pipeline for optimised determination of elastic modulus (E) and Poisson's ratio (ν) in the VEP using DVC data (see Fig. 1). There are two main reasons for establishing a rat L4/L5 lumbar segment FEM. Firstly, it will allow the impact of variable material properties on VEP biomechanics to be examined in a complex system with spinal components, providing a platform for optimising combinations of VEP elastic modulus and Poisson’s ratio. Secondly, it will permit simulation of experiments under a variety of loading and disease conditions, which relieve inherent limitations of the original imaging, thus offering many routes via which VEP mechanical responses can be elucidated, including their behaviour under different postures and degrees of degeneration. Briefly, three separate initial inputs were provided to the optimisation pipeline: 1) an image-based rat L4/L5 lumbar FEM mesh with high resolution microstructures obtained from static sCT scans; 2) DVC strains obtained from *in situ* quasi-dynamic sCT scans; and 3) default VEP isotropic elastic modulus and Poisson's ratio values from literature as a starting point of optimisation. The optimisation pipeline determined the optimal combination of elastic modulus and Poisson's ratio in the VEP, which is an output giving the smallest root-mean-square error (RMSE) between FEM predictions and DVC strains. We found that the robustness of this pipeline was improved via spatially registered node-to-node comparison of FEM predictions with DVC experimental results. This resulted in FEM strain predictions that were comparable to DVC measurements, both within caudal VEP, which was used in optimisation, and the cranial VEP which acted as unseen test data, thus confirming the efficacy of the new pipeline.

Via applying the optimal material properties in the VEP, we validated the utility of this optimised rat L4/L5 FEM by its capacity to simulate VEP macrostructures for load absorption under different spine motions. To extend its application, we simulated distinct disease conditions which revealed how either excessively high or low bone mineral density may trigger IVD degeneration.

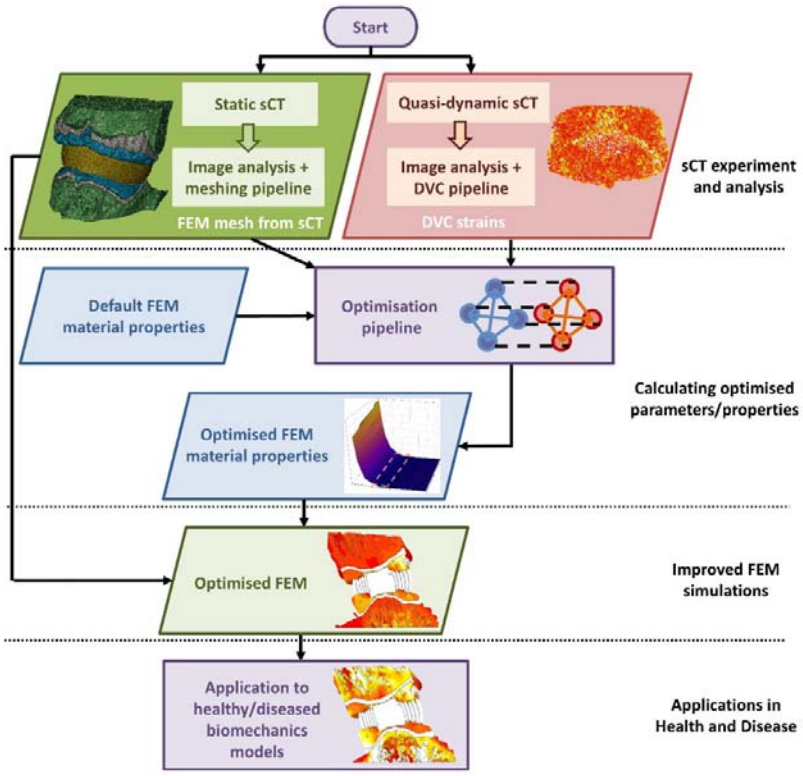

Fig. 1. Workflow of the methods.

Establishment of a rat L4/L5 lumbar segment finite element model

A model comprising vertebrae, growth plates, VEPs, five annulus fibrosus (AF) layers and nucleus pulposus (NP) (Fig. 2, C-E) was constructed. This necessitated a trade-off between capturing very fine detail and computational resources, which was achieved by application of a binning strategy which merged very small trabeculae (~10 μm), but preserved larger trabeculae (~50 μm), together with vertebral and VEP morphological features. Model geometry was initially defined from a vertebral joint, comprised of the L4 and L5 vertebrae and IVD. The joint was placed in a loading rig (Fig. 2, A and B) with a 1N pre-load applied, and then a synchrotron tomographic scan (sCT) with a resolution of 1.625 μm was taken at Diamond Light Source Beamline I13-2. The scan revealed (Fig. 2, B and E) multiple protrusions (which are significant in rodents but not in humans) within the VEP macrostructure and identified 25-30 AF layers depending on location. The bone protrusions were fully resolved in the model, but the AF layers were simplified to a five-layer lamellar structure (each thickened by a factor of five, see Fig. 2F) with an alternating ± 60° orientation homogeneous within each layer (Fig. 2G).

To ensure mesh density would not affect FEM predictions, a mesh-convergence analysis was conducted on both cranial and caudal VEPs. Using coarse (5,021 elements) to fine (162,291 elements) meshes it was found that average first principal strains diminished steeply, by ~16%, in the caudal VEP before attaining a plateau at <72,383 elements (Fig. 2H), which was primarily due to enhanced grid resolution and resultant high strain concentration in the thin VEP central region. First principal strains adhered to a consistent pattern, independent of the

number of elements, except for a scattering of high-strain spots where mesh irregularities generated fine trabeculae that concentrate stress locally within the complex geometry (Fig. 2I). Therefore, an element number of 72,383 with an average size of 52.6 μm was considered converged in the caudal VEP. A similar mesh density was applied to all other components, resulting in a L4/5 lumbar FEM simulation containing 1,316,817 elements, creating a robust FEM platform for simulations.

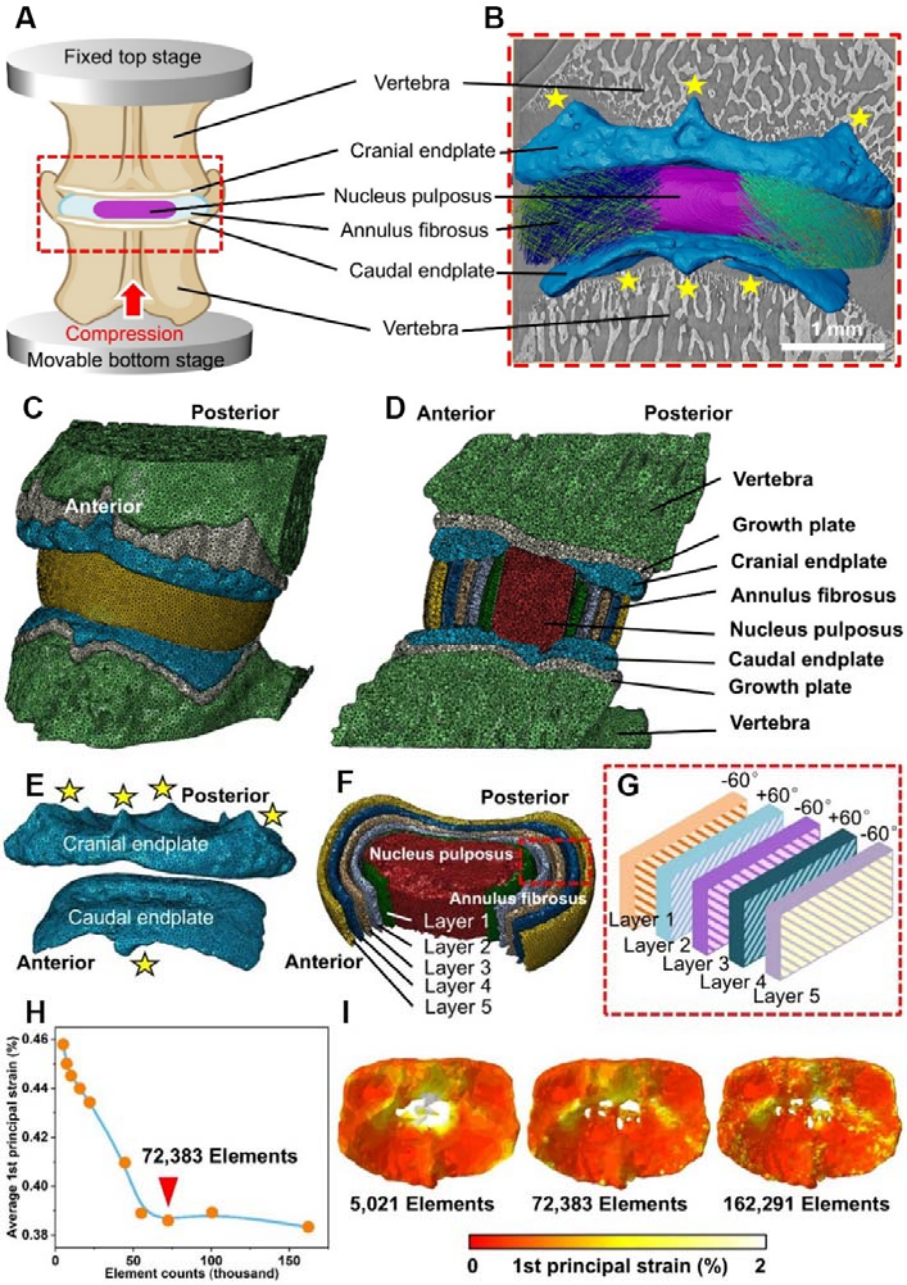

Fig. 2. FEM and caudal VEP grid convergence study. (A) Experimental setup. Rat L4/L5 lumbar segments were mounted onto the Deben CT500 stage. The red dashed line indicates the scan area. **(B)** Grayscale sCT ortho-slice of vertebrae integrated with 3D reconstructions of the VEPs, AF, and NP (Stars indicate the identified protrusions, scale bar = 1 mm); **(C)**

integrated FEM of rat L4/L5 lumbar segments generated from (b), showing **(D)** cross-sectional view; **(E)** isolated FEM of VEPs (Stars indicate the identified protrusions); **(F)** isolated FEM of NP and multilayer AF. The red dashed line box shows **(G)** the alternating ± 60° anisotropic material orientation of each layer; **(H)** mesh convergence study on the caudal VEP showing the correlation between the average first principal strains and the numbers of elements. There are negligible changes in the average first principal strain after exceeding 72,383 elements (red arrow); and **(I)** first principal strain patterns with different numbers of elements.

Spatial registration of DVC correlation point clouds to FEM nodes

To enable optimisation, a DVC reference point cloud for the VEPs was created that could be spatially paired without error with FEM, it was necessary to use identical node numbers and spatial locations. As these were originally non-identical, we created a new reference mesh allowing point-to-point pairing of DVC data with FEM predictions (Fig. 3A and MATERIALS AND METHODS). Use of accurate RMSE evaluation(*29*) confirmed that 91.7% of FEM nodes were within the DVC point domains; this allowed use of a cubic spline interpolation method – a smooth curve-fitting method using third degree polynomials between data points – to map DVC data onto FEM nodes (Fig. 3B). As simple linear extrapolation may lead to error accumulation, nearest extrapolation was applied to the remaining 8.3% of FEM nodes (Fig. 3C) and, after registration, this generated a new DVC point cloud with identical node numbers and spatial locations as FEM; statistical analysis found that this only contained a small amount of divergent low-strain data (Fig. 3D). Direct observations demonstrated that the spatially registered DVC point cloud retained the original strain distribution features, with the same up-side-down 'Y' strain concentration pattern (dashed lines in Fig. 3E), thus confirming that this optimisation pipeline using RMSE evaluation, ensures a reliable reference for the VEP FEM.

Automatic global optimisation pipeline for adjustment of VEP material properties

To yield the smallest FEM predictions and DVC differences utilising minimum RMSE, bespoke codes were created in an automatic pipeline that adjusted VEP material properties using first principal strain as an indicator (fig. S1); a global toolbox (MATLAB) and descent-based algorithms were used. By varying elastic modulus/Poisson's ratio combinations we generated 104 local minimum RMSEs and a global minimum RMSE corresponding to a $E = 67.931$ MPa and $\nu = 0.215$ combination (Fig. 4, A and B). As human, but not rat, spine FEMs containing bony components are already described (fig. S2 and table S1), these were used for comparison. From this we found that rat VEP have an estimated Poisson's ratio/elastic modulus lower than human. Comparability of this optimised FEM and DVC point cloud reference for the caudal VEP was verified with a Bland–Altman comparison(*30, 31*) which exhibited 95.9% agreement (15,584 nodes, Fig. 4C), with poorer agreement only at higher average strain (Fig. 4D). To verify FEM spatial accuracy, average first principal strain in six

subvolumes was subjected to regression analysis to show strong spatial correlation (R^2 = 0.8126, Fig. 4, E-F), indicating that this FEM reached good consistency.

FEM visualisation of first (tension) and third (compression) principal strains demonstrated greatest deformation in the posterior compartment of the caudal VEP; notably in the protrusions on the vertebral side (fig. S3, A-C). These protrusions likely serve multiple functions, including: i) providing greater surface area for load distribution to reduce risk of stress concentration that may cause damage, ii) anchoring the VEPs more securely to the vertebrae to enhance overall stability of the lumbar segment, and iii) maintaining structural/functional segment integrity by deforming under load to distribute strain more evenly on the IVD. These possibilities will be explored in our model.

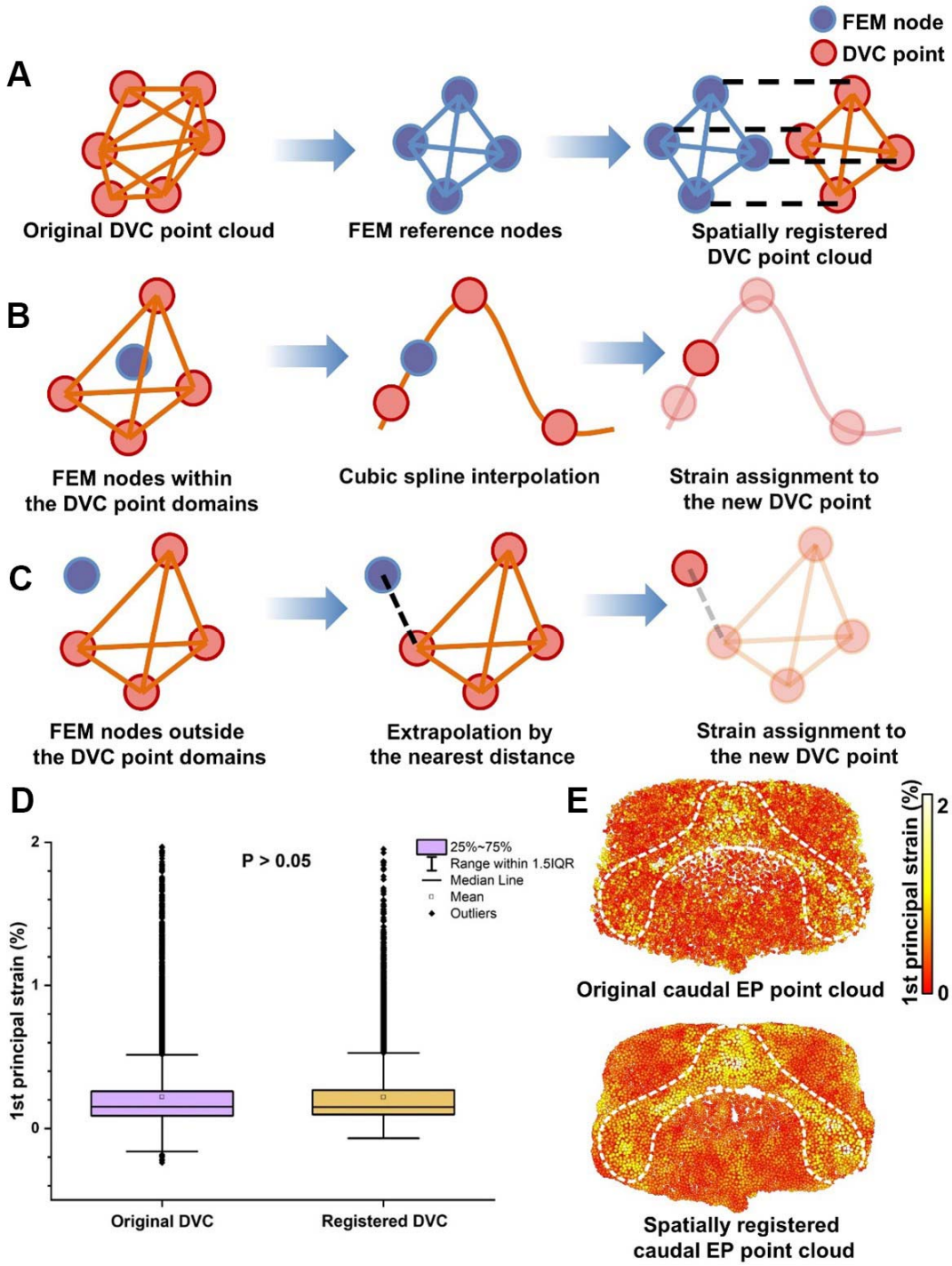

Fig. 3. Spatial registration of the DVC point cloud to FEM reference nodes. (A) Cubic spline interpolation method for new FEM-referenced DVC points within the original DVC point domains; **(B)** extrapolation method for new FEM-referenced DVC points outside the original DVC point domains; **(C)** spatial registration of the DVC point cloud; **(D)** statistical analysis of the first principal strain values between the original and registered caudal VEP point clouds. P > 0.05; and **(E)** visualisation of the first principal strain in the original and

registered caudal VEP point clouds. Dashed lines indicate the regions of concentrated first principal strain.

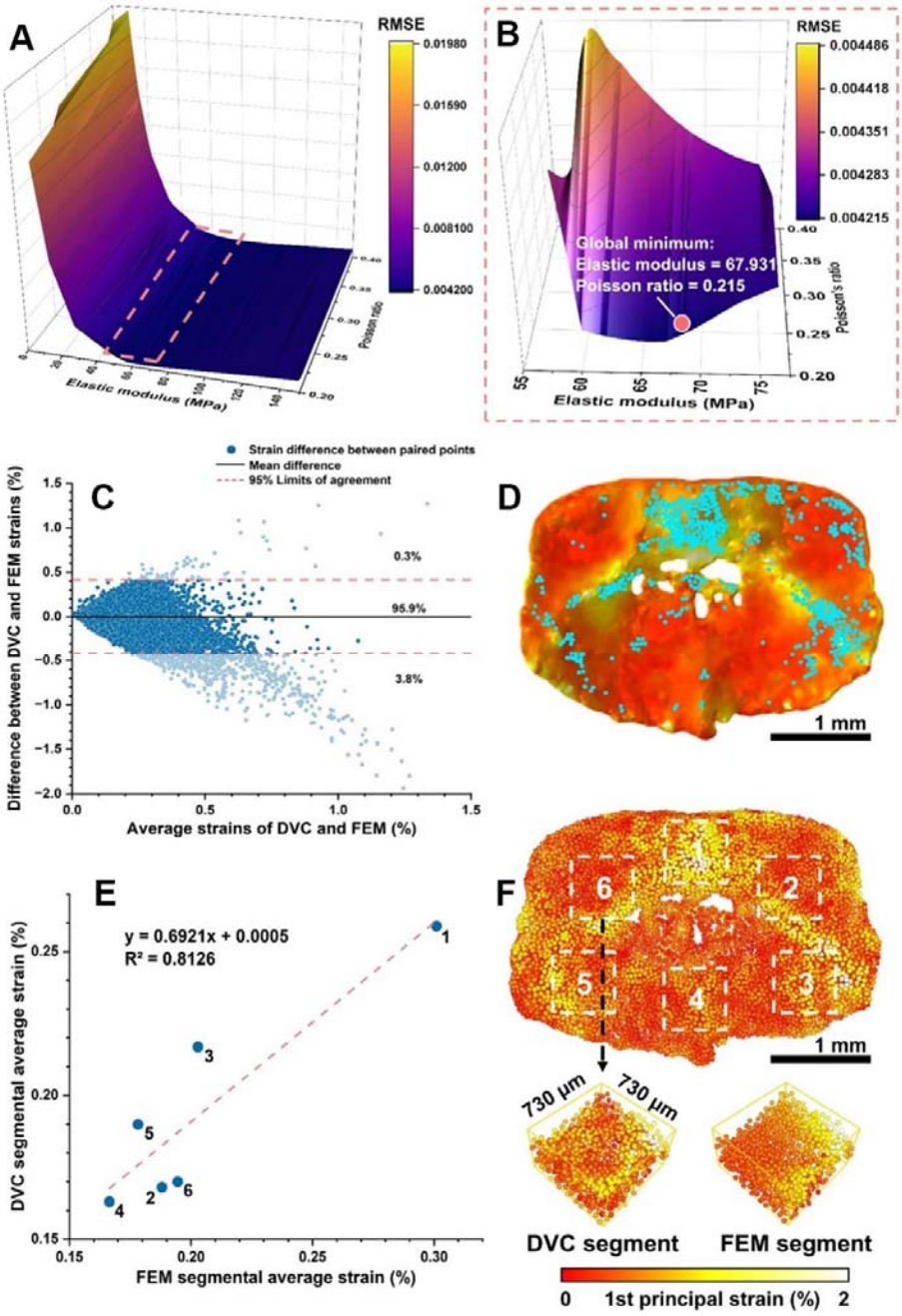

Fig. 4. Global optimisation of material properties of caudal VEP and statistical analyses. **(A)** Visualisation of the correlation between the first principal strain RMSE and combinations of the elastic modulus and Poisson's ratio. The red dashed box indicates **(B)** the zoom-in view of the location of the global minimum RMSE; **(C)** the Bland–Altman plot showing the deviations of first principal strain between FEM predictions and DVC measurements. The unit (%) on the x and y axes refers to the first principal strain values. **(D)** Visualisation of the locations of underestimated FEM predictions. Each cyan dot represents an FEM node. **(E)**

Regression analysis of first principal strain between subvolumes of FEM and DVC; **(F)** Locations for subvolume extraction. The size of each subvolume was 730 μm × 730 μm × 730 μm. (Scale bars = 1 mm.)

Validation of the optimisation pipeline

Validating FEM accuracy using experimental data is essential prior to its predictive usage. Therefore, once FEM-predicted first principal strain was matched to DVC measurements in the caudal VEP, we validated the optimisation pipeline efficacy by longitudinally comparing FEM/DVC first and third principal strains on caudal/cranial VEP from the preload (1N) to three loading steps (4, 8 and 12% strain of full IVD height). We targeted a strain difference of less than 10%(*32*) between FEM and DVC and achieved it. Specifically, although optimised using only first principal strain at the second loading step (8% compression), FEM in the caudal VEP also generated accurate predictions at 4 and 12% compression (Fig. 5A and Table 1). Specifically, if the percentage difference between the means of the distribution of first principal strains from FEM and DVC are calculated, the difference is very small (e.g. 5.2% percentage difference at step 3) (table S2). Likewise, FEM predicted similar third principal strains to the DVC point cloud reference in the caudal VEP across all three load steps (Fig. 5B and Table 1), with a maximum percentage difference of 5.1% at step 3 (table S2). This indicates that the node-to-node RMSE-based global optimisation algorithm provides near-identical mean strain values for FEM and DVC. This correlation in strain pattern and macrostructure aligned with visual inspection of FEM and DVC data from the caudal VEP (Fig. 5, C-D).

Strain prediction accuracy in this experimental set-up is likely more challenging in the cranial VEP, as it is not only affected by the loading step and optimisation algorithm but also by the load transfer system and anatomical interactions. Remarkably, FEM performance in the cranial VEP was similar, with both first and third principal strains (Fig. 5, E-F and Table 1) displaying similar statistical distribution to DVC data at each loading step; e.g. maximum percentage difference in mean first and third principal strains between DVC and FEM were 5.5 and 5.4%, respectively, at step 2 (table S2). A Visual inspection revealed that cranial VEP FEM predictions exhibited a similar strain pattern to DVC (Fig. 5, G-H and fig. S4).

The most deformed caudal and cranial regions were opposing in the anterior-posterior direction, suggesting that the VEP is not only responsible for load absorption but also alters load direction through the AF-VEP junction and AF fibre bundles; this premise requires further investigation. FEM in both caudal and cranial VEP were, however, partially inconsistent with DVC in the high-strain regions, with 3-4% of the predictions significantly underestimating the first principal strain (Fig. 4C), but with a strong correlation still retained at all loading steps (Bland–Altman, > 95%, Table 1). This displays enhanced FEM accuracy through use of DVC data and confirms method reliability in simulating VEP biomechanical behaviours.

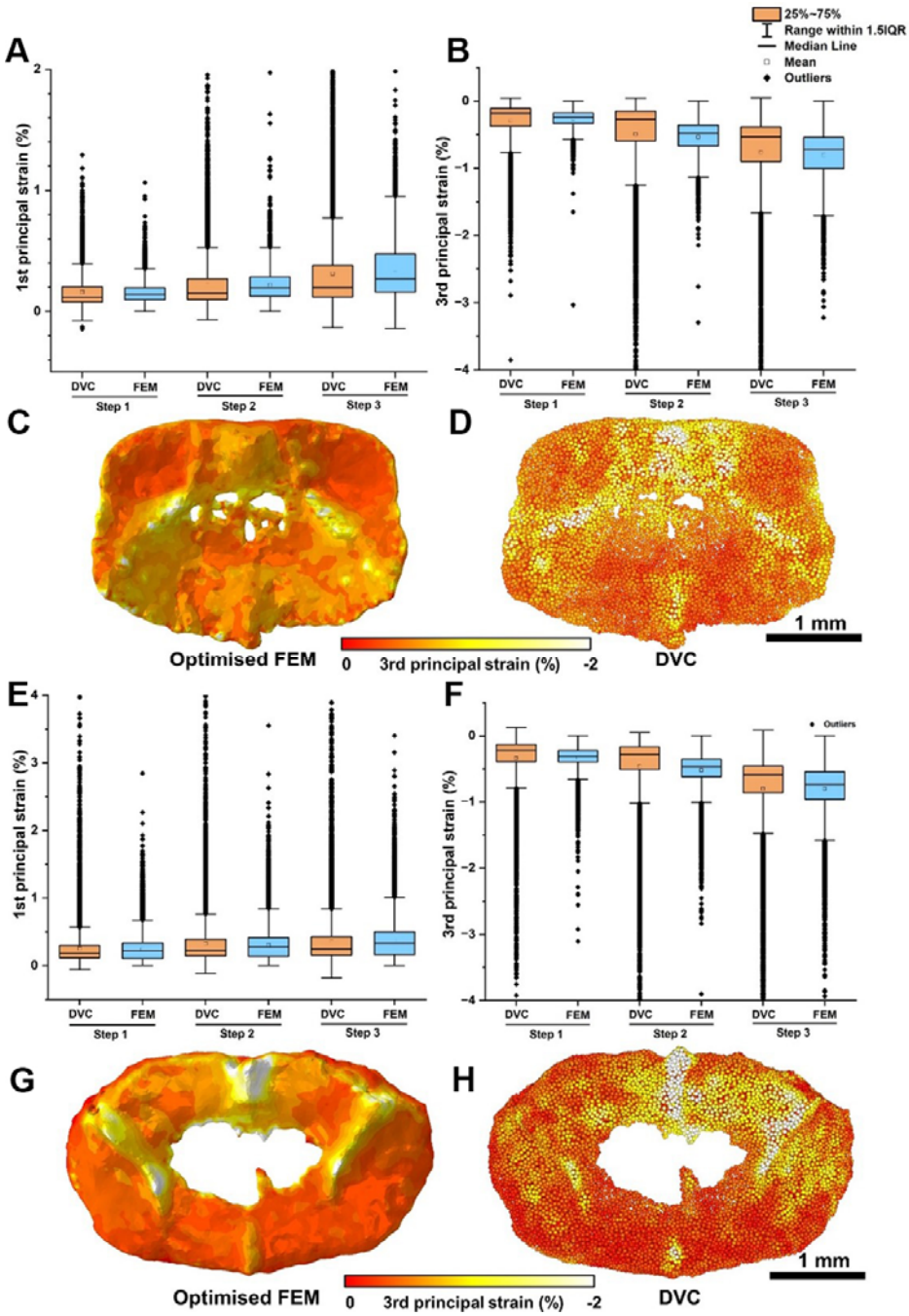

Fig. 5. Strains on caudal and cranial VEPs. Statistics of **(A)** first principal strain and **(B)** third principal strain of caudal VEP optimised FEM and DVC point cloud reference at different loading steps; visualisation (bottom view) of third principal strain on caudal VEP **(C)** optimised FEM and **(D)** DVC point cloud reference at the second loading step (under 8% remote compressive strain). Statistics of **(E)** first principal strain and **(F)** third principal strain of cranial VEP optimised FEM and DVC point cloud reference at different loading steps; Visualisation (top view) of third principal strain on cranial VEP **(G)** optimised FEM and **(H)** DVC point cloud reference at the second loading step (under 8% remote compressive strain). (Scale bars = 1 mm.)

Samples	Type of strain	Compression steps	Nodes within 95% limits of agreement (%)	Overestimated nodes (%)	Underestimated nodes (%)
Caudal VEP	First principal strain	1	95.1	0.8	4.1
		2	95.9	0.3	3.8
		3	95.6	1.2	3.2
	Third principal strain	1	95.1	0.1	4.8
		2	95.5	0.1	4.4
		3	95.4	0.5	4.1
Cranial VEP	First principal strain	1	95.7	0.7	3.6
		2	96.4	0.4	3.2
		3	96.0	0.6	3.4
	Third principal strain	1	95.7	0.2	4.1
		2	96.0	0.2	3.8
		3	95.2	0.7	4.1

Table 1. Statistics of the Bland Altman plots at different compression steps.

Note: Step 1: 4% remote compressive strain; Step 2: 8% remote compressive strain; Step 3: 12% remote compressive strain.

Associations between endplate macrostructures and biomechanics

A primary application of this optimised FEM is to expose key functional VEP macrostructures. It is therefore intriguing that the protrusion macrostructures on both the posterior caudal and anterior cranial VEP regions experienced concentrated first/third principal strains. The reconstruction of VEP macrostructures in sCT scans disclosed paired sagittal and lateral 'interlocking' protrusions on the surface of adjacent caudal and cranial vertebral VEPs (Fig. 6A). These VEP protrusions (red) are short and straight, and positioned anteriorly and posteriorly along the sagittal plane, whilst those positioned laterally (blue) are elongated to form a ~25° and ~35° angle to the sagittal plane for the cranial and caudal VEP, respectively. The sagittal protrusions are more pronounced, and all four are taller in the cranial than the caudal VEP. These findings infer that mechanical function differs in these regions and they pose questions about the roles of these protrusions in multiaxial motions of rat spines. This aligns with the concentration of strains to protrusions under uniaxial compression (Fig. 5G and fig. S4) and infers roles in load absorption and redistribution.

To interrogate protrusion biomechanics, we used FEM to simulate spinal motions and evaluated the resultant strains in a preload step (1N, equivalent to ~1/3 body weight; to provide a baseline for quadrupedal posture) and then at 13° flexion, 2° extension, 6° lateral flexion and 2° rotation positions to simulate the physiological motion range in the L4/L5 lumbar segment(*33*) (Fig. 6B). FEM showed that the sagittal and lateral protrusions retained most deformation even though its range varied under the different motions. Thus, sagittal-

plane flexion and extension generated greater shear strain in sagittal than in lateral VEP protrusions, whilst lateral-plane flexion and rotation, yielded greater shear strain on the horizontal plane of the lateral VEP protrusions (Fig. 6C). These data suggest that sagittal protrusions serve roles in load absorption and transfer under sagittal spine motions, while lateral protrusions balance the load from lateral flexion/rotation by deforming. Together these VEP macrostructures thus stabilise the spine in multiaxial complex motions.

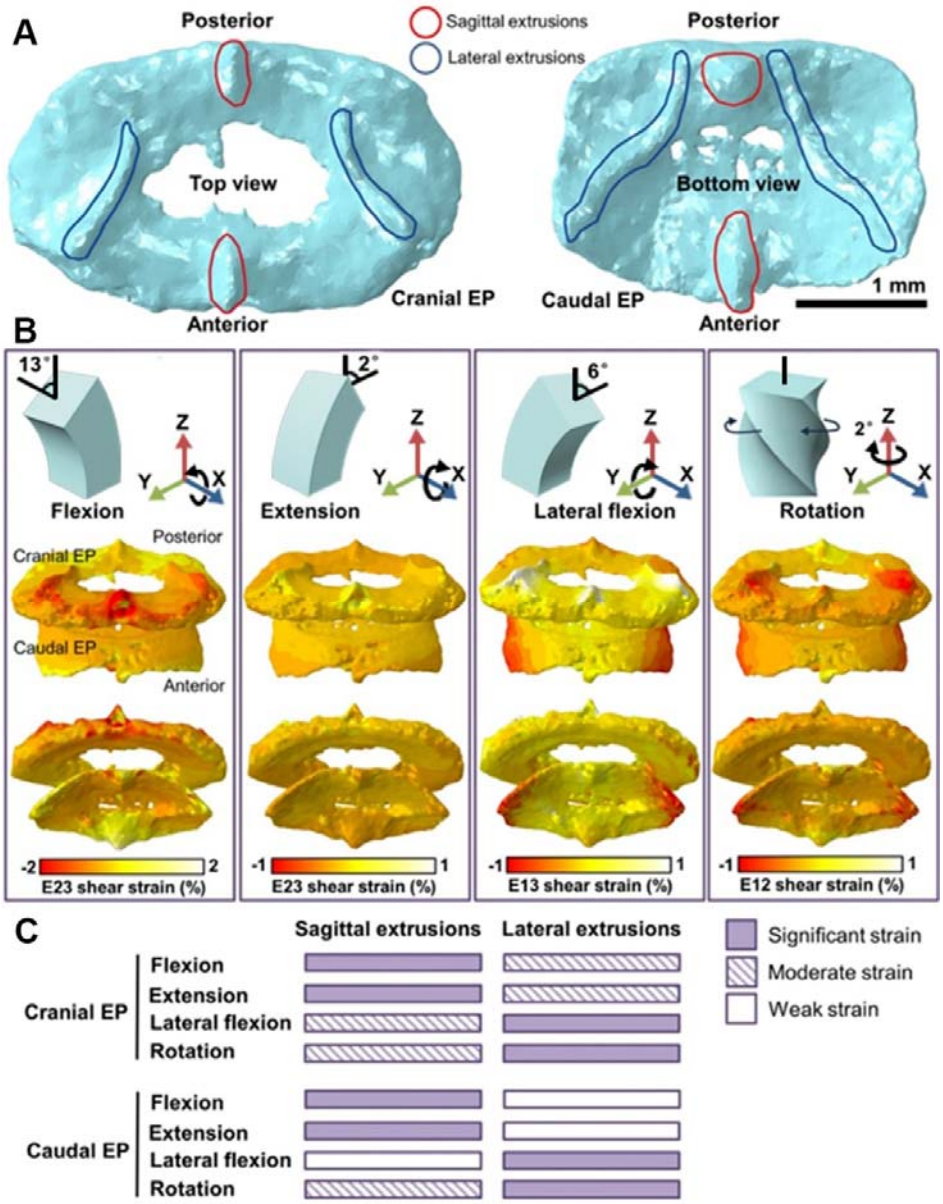

Fig. 6. **Associations between VEP macrostructures and biomechanics. (A)** Sagittal and lateral protrusions identified on cranial and caudal VEPs. Red circles indicate sagittal protrusions, while blue circles indicate lateral protrusions. Scale bar = 1 mm; **(B)** Shear strain distributions on sagittal (E23), coronal (E13), and horizontal (E12) planes of cranial and

caudal VEPs under different motions; **(C)** Significance of strains on sagittal or lateral protrusions of VEPs under different motions.

Impact of VEP on IVD under diseased conditions

Our optimised FEM may also allow simulation of how disease-affected VEP/vertebrae contribute to IVDD. To test this, we use our FEM to interrogate if biomechanical mechanisms underpin the U-shaped model proposed by Kague *et al*., to describe the link between bone mineral density (BMD) and IVDD(*34*); in the absence of any in-depth biomechanical analyses, it has been suggested that IVDD may develop in both the transcription factor Sp7 knockout zebrafish model, which represents osteoporosis (OP), and the cathepsin K mutant zebrafish model, which represents pycnodysostosis (PYCD). This model speculates that both low and high bone mineral density could be responsible for IVDD in these mutant zebrafish. To explore this speculation, we created two modified rat L4/L5 lumbar FEMs to simulate OP and PYCD lumbar segments (Fig. 7A). The former simulates trabecular thinning in vertebrae and a reduced elastic modulus in both vertebrae and VEP(*35*), while the latter retains vertebral and VEP trabecular microstructure(*36*), but simulates an increased elastic modulus(*37, 38*).

Using our models, we found that application of identical 3N load (equivalent to 100% rat body weight) engendered higher vertebral/VEP strains and lower IVD strains in the OP model than in other conditions (Fig. 7, B-C). Remarkably, these shifts in the OP model were linked to marked increases in third principal strain in the four VEP protrusions (versus healthy FEM, Fig. 7D) and poorer load transmission capacity to the IVD. In contrast, loading of the PYCD model propagated divergent biomechanical behaviours, in which compressive strains were greater in the IVD due to a diminution to load transfer across the stiffer VEP and via deformation of the four VEP protrusions (Fig. 7C-D). Closer inspection of FEMs in the IVD showed a homogeneous reduction in first principal stress in the OP model, compared to the healthy spine (by about ~67%) (Fig. 7E). Notably, load application in the PYCD model engendered significantly greater (179%) first principal stress in the IVD mostly in the NP and less so in the AF (109%), suggesting that IVD strain and stress are sensitive to changes in VEP material properties.

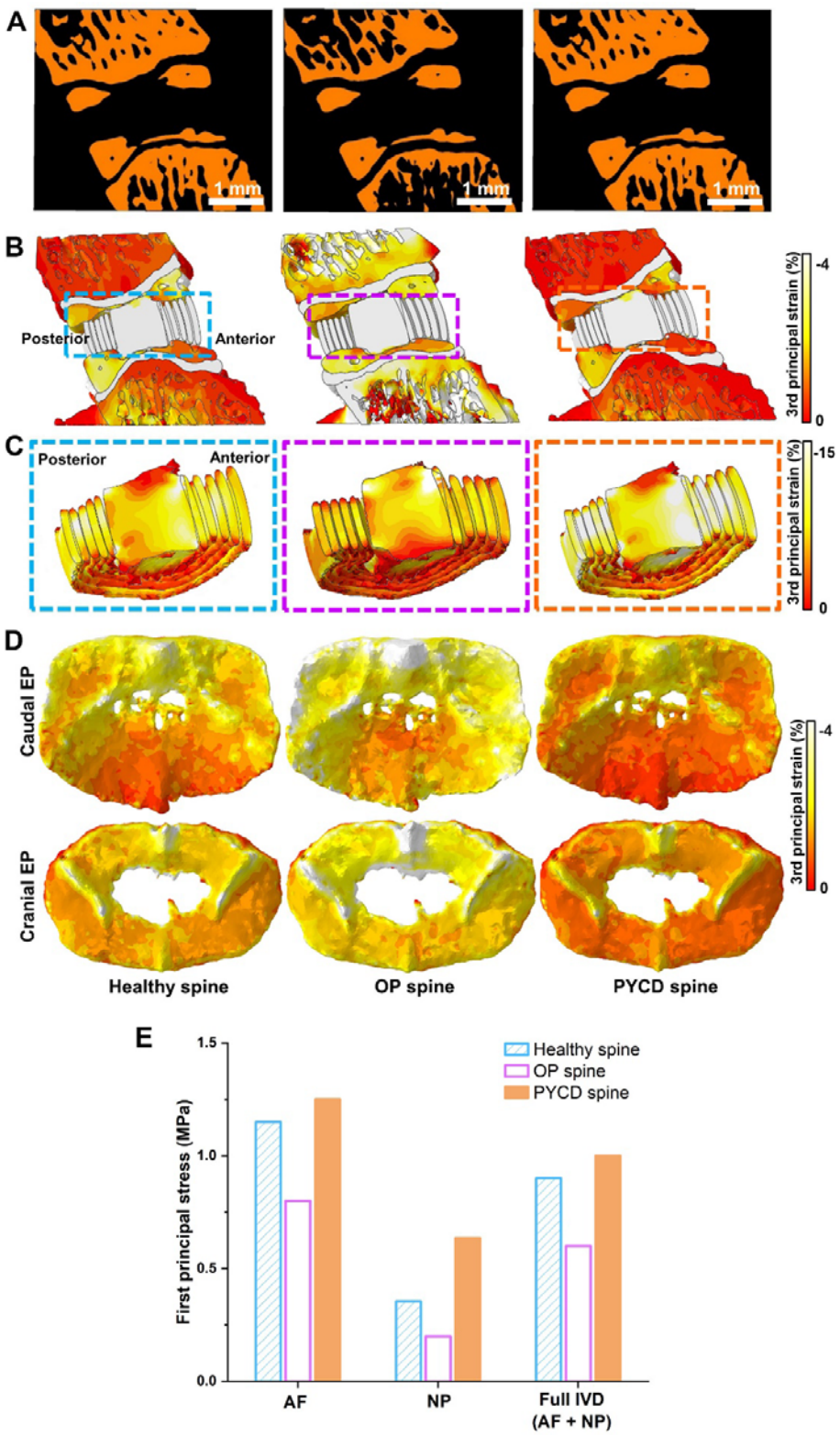

Fig. 7. Simulation and comparison of healthy spine, OP, and PYCD FEMs. (A) Orthoslice of lumbar FEMs under different conditions. Scale bar = 1 mm; visualisation of third principal strain on **(B)** the entire L4/L5 lumbar FEM, **(C)** IVD, and **(D)** cranial and caudal VEPs; and **(E)** statistics of average first principal stress on different parts of the IVD.

DISCUSSION

This study was focused on rat vertebral VEPs that were used to validate our FEM optimisation pipeline. Our data indicate that DVC measurements enhance FEM prediction accuracy to reveal functional VEP macrostructures linked to specific spinal motions. The new FEM pipeline utility was additionally validated via its elucidation of likely biomechanical mechanisms underlying osteoporosis (OP) and pycnodysostosis (PYCD), illustrating how these conditions influence VEP biomechanics to initiate IVDD.

The combination of high-resolution sCT, DVC and *in situ* mechanical testing has exhibited novelty in quantifying 3D full-field nanoscale strains(*12*). In orthopaedics, this approach has been applied to mouse Achilles tendon entheses(*39*), whole femurs(*40*) and whole knee joints(*12*), rat whole lumbar IVDs(*16, 17, 19, 41*) and tibial plateaus(*42*), cuttlebone cubes(*43*), bovine tibial(*43*) and femur(*43-47*) cylinders, knee joint articular cartilage and medial meniscal(*48*), sheep femoral condyle cylinders(*49, 50*), human thoracic vertebrae cylinders(*51*), femoral head cylinders(*52-54*), and whole proximal femurs(*55*). Although such sCT imaging can resolve exceptional structural detail, and DVC use is invaluable in showcasing local vs global strains, most of these studies have only investigated relatively small and homogeneous samples. Application of sCT-based *in situ* DVC in intact joint biomechanics, including both soft and hard tissues, is still at an early stage. To our knowledge, intact rat spine studies utilising sCT-based *in situ* DVC have only been reported by Parmenter *et al*.(*17, 56*) and Disney *et al*.(*16, 19, 41*). The latter elegantly resolved structural responses in collagen bundles to increasing uniaxial compressive load to report differences in AF compliance in different IVD regions(*19*), and the former showed that local strain distribution varies regionally at AF-EP junction, and relationships between microstructure and mechanics, nanoscale mineral structure, and molecular level prestrain in VEP. Neither, however, explored full-field VEP function or mechanics under multiaxial motions or diseased conditions, emphasising that this is still required.

Despite the advantages of sCT-based *in situ* DVC, bidding processes and long waiting times deter access to sCT facilities(*57*). Bespoke sample holders for *in situ* mechanical load application also need to be designed and manufactured and, with cost and size of a multiaxial mechanical tester, it is not surprising that our experiments were all performed on simpler uniaxial compression/tension devices. sCT-based *in situ* DVC is also limited by animal model availability. It is likewise important to appreciate that the rat model studied herein may not have direct translation to humans(*58*) and it is generally acknowledged in bone research that larger sheep and dogs, more closely resemble human biomechanics and pathology(*59*). These are often more expensive requiring complex housing facilities and management, which limits their use. For these reasons, FEM has promise in providing new insights into VEP biomechanics, as it not only allows elucidation of global VEP strain/stress but can also simulate the influence of different motions and disease conditions without much additional investment.

Material properties significantly affect FEM prediction accuracy. Thus, one of our aims was to develop a pipeline allowing material properties of a complex rat VEP to be adjusted in line

with DVC data. This would address the lack of a human spine FEM to measure the elastic modulus and Poisson's ratio of individual IVD components, and thus justifies use of human spine material properties in our rat lumbar FEM as a reasonable starting assumption. Existing data for apparent moduli from mouse(*60*) and rat(*60, 61*) spine segments are indeed in the same order of magnitude as human(*60*) and, while some studies have reported similar inverse methods on homogeneous materials(*25, 26*), this is the first to apply this method to an intact joint. Our pipeline also affords an advance in its use of a full-field node-to-node spatially registered reference and its scope to vary material properties.

Spatial registration in our FEM integrates varied 3D strain values in different VEP regions, while identifying global elastic modulus/Poisson's ratio in RMSE from local optima. Interestingly, the material properties used in prior FEM studies (fig. S2 and table S1) of humans exposed marked inconsistencies in properties both within and across spine segments (fig. S1). Comparing the outcomes of our pipeline with reported human VEP material properties, we find that global optimal values for the rat VEP elastic modulus falls within the human VEP range (68 MPa vs. 24-1,200 MPa) while Poisson's ratio is slightly lower (0.215 vs. 0.25-0.4). It is vital, however, to highlight that determination of these parameters is complicated by the inhomogeneous, anisotropic, viscoelastic, and nonlinear(*62*) properties of biological tissues. Determination of VEP material properties can be further obscured by sample selection (spine segments, donor age) and preparation, measurement standards (macroscale properties(*63*), microscale indentation(*64*), or BMD-dependent CT grayscale prediction(*64*)) and region measured(*65*). Such factors can clearly contribute to significant variation between studies. Importantly, our optimal VEP material properties resulted in good statistical and spatial consistency of strains with DVC data to validate the robustness of our FEM in the unsupervised strain prediction in this complex load transfer system.

We noted that FEM predictions had 3–4% strain values above/below the 95% limits of agreement with DVC data. This may reflect differences between FEM and DVC algorithms, as DVC tracks the natural microstructure-related grayscale values in the sample and calculates the displacements in only small subvolumes(*66*). Previous studies have reported a load-induced crack development and failure of fine trabeculae (~100 μm) leading to significantly raised DVC values(*67*). Our FEM was informed by binned sCT images that averaged fine trabeculae which, in contrast, did not consider damage, and thus will not be able to predict failure, and whilst failure has been reported to occur with similar ~1% compressive strain in bovine and human trabeculae(*68*), this plastic modulus was not included in our FEM due to a lack of data in the rat. These factors may explain the lack of extremely high >1% strains from our datasets (Fig. 4D) and underlines that our FEM does not capture all biomechanical behaviours but instead estimates physiology closely using only moderate computational power (e.g., runnable on personal laptops, whereas DVC requires workstations or computer clusters). The optimised pipeline was indeed effective in a complicated system composed of ‘interacting’ parts with divergent material properties and can use material properties from humans. DVC-based FEM material property optimisation could further improve the range of strain values and their spatial distribution, which is critical for more detailed and robust analyses in different species and individual parts of the spine.

By simulating diverse motions, our FEM simulations also support links between VEP macrostructure and dynamic spinal biomechanics. These relationships have hitherto remained poorly understood due to the limitations of CT resolution. A few studies in human samples have reported an uneven distribution of stiffness(*69*) and strength(*69, 70*) in different VEP regions, which follow bone remodelling principles(*71, 72*), and shear stress transfer via AF branched anchorage at the AF-VEP junction(*11*). Two animal studies visualized the morphology of VEP in mice(*73*) and rats(*74*) in a static state but did not clearly describe the VEP protrusions. None of these studies have, however, linked any architectural features to efficient motion and, whilst VEP morphological lesions are clearly correlated with IVDD(*8, 75*), the underlying mechanistic relationships remain undefined. In this study, we use FEM to offer mechanistic links between protrusions on the vertebral side and load absorption and redistribution during specific motions. This emphasises the strength of our pipeline and highlights that VEPs are not only inhomogeneous in thickness, stiffness, and strength but also have different functional regions that are integral in maintaining rat spine stability during complex multiaxial motions. Malformation or lesions of these macrostructures may impair local spinal biomechanics and cause concentrated IVD strains, accelerating IVDD. They may also be utilised in predicting IVDD development and their reconstruction may be important in surgery. Our interrogation of these VEP protrusions suggests a role in the load transfer path through compliant AF collagen bundles(*19*), which is worthy of further investigation.

To extend application of our optimised rat spine FEM, we sought evidence for its predictive capacity in two clinical conditions that align with a model which speculates that both low and high BMD are biomechanically detrimental in the IVD(*34*)'(*76*). Application of our FEM to OP and PYCD indeed offer support for its broader utility. Lower modulus and more porous vertebral trabecular bone in the OP model aligned with reduced first principal stress throughout the IVD, which may reflect an insufficient mechanical stimulus, related to compromised oxygen and nutrient supplies and the onset of IVDD. In contrast, the PYCD model with pathologically high elastic modulus in vertebrae and VEPs predicts extremely high (179%) first principal stress in the NP, which may exceed physiological thresholds(*77*). Data from our new FEM imply that low or high BMD triggers IVDD by distinct modes and hence require alternative interventional approaches.

There are limitations in this study. To balance accuracy and computation, the FEM was established based on the sCT images binned by four. This caused inevitable merging of some fine trabeculae (~10 μm) into larger structures (~30 μm) and thus less concentrated strains. A highly detailed model should be created and run on a computer cluster for comparison in the future. The hyaline cartilage endplate has not been included in the model as an in-depth study of its biomechanics are beyond the scope of this manuscript. The FEM included only the isotropic elastic modulus and Poisson's ratio, while plasticity and damage under load were not considered due to a lack of experimental data. The IVD part of the FEM is more simplified than other parts. Although lamellar structure and anisotropic orientation were considered, they did not completely resolve the individual AF collagen bundles and their varied orientation within the same lamella(*19*), which limited us to further studying interaction at AF-VEP junctions and the load transfer path from one VEP via the collagen

bundles to another. The regional variation of AF orientation within the same lamella was not considered. Our predictions on different motions, OP and PYCD models were based on computations and data from literature, and more experimental validations are needed to confirm our findings. It should also be noted that VEP structure differs among species(*78*) and that rodents and humans have distinct forms of locomotion. Hence, more consideration should be given when animal models are used to study human diseases.

Overall, our study established a global pipeline for optimising the material properties of rat lumbar VEPs in an intact spine motion segment FEM. The optimised FEM displayed strain values and distributions in good agreement with the DVC measurements. Functional macrostructures linked to different motions were identified on both cranial and caudal VEPs. The FEMs of the diseased states (OP and PYCD) demonstrated the potential of studying musculoskeletal degeneration utilising the optimised FEM. Although we demonstrated these methodologies on small animals, they are scalable to large animals and humans.

MATERIALS AND METHODS

In situ sCT, image reconstruction, DVC, and FEM of the rat L4/L5 lumbar segment

In situ sCT, image reconstruction, and DVC of rat L4/L5 lumbar segments were performed based on our previously established methods(*16, 17, 19*). Briefly, the sCT scans generated high-resolution images of rat L4/L5 lumbar segments with a voxel size of 1.625 μm at initially a preloading step (1N, equivalent to ~1/3 of the animal's body weight), followed by three loading steps (4%, 8%, and 12% strain of full height of IVD)(*79*). The field of view captured approximately 1 mm each of the L4 and L5 vertebrae, and the entire VEP and IVD. The reconstructed images were first binned by four using Avizo 3D (v. 2022.2, Thermo Fisher Scientific, Waltham, US). After that, the segmentation module in Avizo 3D was used for segmenting the volumes of the vertebrae, growth plates, and VEPs. The segmentations were then converted into surface data with a simplified minimum edge length of 32.5 μm. In terms of AF and NP, 3D models of five AF lamellae and an NP were created according to their boundary and shape in the sCT images using Cinema 4D (v. 2023, Maxon, Bad Homburg, Germany) and exported as STL files. After that, the STL files were imported into Avizo 3D and underwent the same simplification process with a minimum edge length of 32.5 μm. After that, together with other surface data, they were all converted into tetrahedral grids. The tetrahedral grids were then exported as INP files adapted to Abaqus CAE (v. 2023, Simulia, Providence, US), which was used to perform finite element analysis on the strain and stress on the spine. After the materials were imported into Abaqus/Standard, the material properties were determined, as detailed in table S3 and table S4. Orientations were also applied to AF lamellae to mimic anisotropy in each lamella (table S4). Our previous work showed that collagen bundles in AF lamellae have alternating ± 30° or ± 60° orientations, depending on their IVD location(*16, 19*). To represent the anisotropic orientation in each lamella, alternating ± 60° material orientations were applied to the AF in the FEM. The parts were assembled into an integrated model according to their original spatial relationship, the corresponding interactions were set to connect the parts, and surface-to-surface contact was

applied between the AF lamellae and the innermost AF lamella and NP (fig. S5). The highest and the lowest planes of the lumbar segment FEM were kinematically coupled with two reference points (RF1 and RF2, respectively) which located at the centre of the planes. All boundary conditions were applied to these two reference points which have constrained all degrees of freedom to the planes. The boundary conditions were the same as those in the experiment. Briefly, RF1 was encastred to replicate the experiment, where the top of the spine segment was glued to the compression stage, while the lowest plane of the caudal vertebra was subjected to compressive displacement via corresponding to 4%, 8%, and 12% (relative to the full height of the IVD) of a remote compressive strain, respectively. Displacements were applied at RF2 along Z direction, with constrained zero displacement in X and Y directions. The strain and stress over the FEM were then calculated and visualised in the implicit solver.

FEM convergence study of VEPs

To avoid the FEM results being affected by the number of elements in the grids, a convergence study was conducted on both cranial and caudal VEPs. A series of tetrahedral elements with different minimum edge lengths (24.4 μm, 28.4 μm, 32.5 μm, 34.9 μm, 37.4 μm, 44.7 μm, 52.8 μm, 60.9 μm, 69.1 μm, and 77.2 μm) were created in Avizo 3D following the description above. They were then exported as INP files and imported into Abaqus CAE to replace the original VEPs FEM. All elements were tetrahedral with four nodes and one integration point. Accordingly, combination material properties ($E = 110$ MPa, $\nu = 0.3$) were initially assigned to the VEP by the MATLAB Global Optimisation Toolbox with boundary condition of 8% remote compressive strain, and static analysis conducted with the implicit solver. After obtaining the strain data on the VEP FEM, the average first principal strain at the nodes was calculated. Plots of the average first principal strain vs the number of elements on both VEPs were generated using Origin (v. 2023b, Originlab, Northampton, US). When the average first principal strain no longer changes significantly with an increase in the number of elements, the critical point is regarded as convergent, and the number of elements after the critical point is used for subsequent experiments.

Registration of the DVC point cloud to FEM nodes

Prior to the global optimisation pipeline, DVC point clouds were registered to FEM nodes via a bespoke code in MATLAB (v. R2023b, MathWorks, Natick, US). The original caudal and cranial DVC meshes contained 23,529 and 29,187 nodes, respectively. First, the original DVC mesh (Mesh 1) was replaced by a new DVC mesh (Mesh 2) with the same node number and node spatial position referenced to the FEM mesh (Mesh 3). On Mesh 2, the nodes were then assigned values of first principal strain from Mesh 1 following two principles: 1) if the Mesh 2 nodes were within the Mesh 1 domains, cubic spline interpolation was used to generate strain values for Mesh 2 nodes; 2) if the Mesh 2 nodes were outside the Mesh 1 domains and cubic spline interpolation could not be applied, extrapolation by the nearest Mesh 1 nodes was performed. To validate the comparability, Mesh 2 was then compared with Mesh 1 on statistical and spatial distributions of first principal strain values.

Global optimisation pipeline

The global optimisation pipeline was established on integrated bespoke codes on the platforms of MATLAB and Abaqus CAE built-in Python. The first principal strain on the caudal VEP was utilised for the pipeline. Fig. S1 outlines the workflow. Briefly, a bespoke MATLAB function was used to modify the elastic modulus and Poisson's ratio of the caudal VEP FEM in the INP file of Abaqus CAE. The adjustment ranges of the elastic modulus and Poisson's ratio were set to [10, 150] MPa and [0.2, 0.4], respectively. Then, the Abaqus Standard was launched, and the INP file containing all the information on the parts, models, interactions, and boundary conditions (8% compressive strain) was imported into Abaqus. After that, a bespoke code was run by the Abaqus built-in Python, which submitted the job to and ran it using the implicit solver. The first principal strain data of the caudal VEP FEM were extracted by another bespoke MATLAB function for comparison with the DVC data in node-to-node form. Deviations from each pair of FEM-DVC nodes contribute to the final RMSE (Equation 1), which reflects the degree of difference between two paired datasets. The MATLAB Global Optimisation Toolbox using gradient descent-based algorithms was used to analyse the RMSE values and determine whether they were the global minimum. Otherwise, the combination of the elastic modulus and Poisson's ratio would be automatically adjusted and rerun above the workflow; otherwise, the global optimisation pipeline would be terminated, and the global optimal combination of the elastic modulus and Poisson's ratio and corresponding RMSE would be printed. The visualisation of the optimisation results in the full range was plotted using Origin.

$$\mathrm{RMSE} = \sqrt{\sum_{i=1}^{n} \frac{(\hat{y}_i - y_i)^2}{n}} \tag{1}$$

where

$\hat{y}$ is the FEM-predicted value.

y is the DVC measured value.

n is the number of node pairs.

Bland–Altman plot

Data normality was tested and Bland–Altman plots were constructed to study the agreement of the first principal strain under 8% remote compressive strain on the caudal VEP between the FEM predictions and DVC measurements. The properties of a normal distribution indicate that approximately 95% of the data points will fall within the mean plus or minus 1.96 times the standard deviation (SD), and a 95% confidence interval offers sufficient information to judge whether two measurement methods have adequate agreement. The Bland–Altman plots were created based on the averages (x-axis, Equation 2) and differences (y-axis, Equation 3) of the first principal strains between the paired FEM and the DVC data, followed by computing the mean and standard deviation of these differences to establish 95% limits of agreement, defined as the mean difference plus or minus 1.96 times the SD(*30, 31*). In the situation where two independent measurement methods have good agreement, over 95% of the data points should fall within the range of limits of agreement. The visualisation of the Bland–Altman plots was performed using Origin.

$$\overline{e_i} = \frac{e_i^{FEM} + e_i^{DVC}}{2}$$
(2)

$$\Delta e_i = e_i^{FEM} - e_i^{DVC} \quad (3)$$

where

e_i^{FEM} is the FEM-predicted first principal strain.

e_i^{DVC} is the DVC measured first principal strain.

Linear regression analysis of subvolumes

Linear regression was performed to analyse the spatial agreement of the average first principal strains between the FEM predictions and DVC measurements under 8% remote compressive strain on the caudal VEP subvolumes. Six paired subvolumes (730 μm × 730 μm × 730 μm cubes) at the anterior, lateral anterior, posterior, and lateral posterior caudal VEP locations were extracted from both FEM and DVC references. The average first principal strains at nodes were calculated, and the agreement was assessed utilising linear regression in SPSS Statistics (v.29.0.0.0, IBM, New York, US) and then plotted utilising Origin.

Comparison between FEM and DVC under different motions

Based on the FEM generated from the preloading step, a series of boundary conditions within the physiological motion range of the L4/L5 lumbar segment were applied to the rat lumbar segment FEM, including uniaxial displacement of 4%, 8%, and 12% remote compressive strain, 13° of flexion, 2° of extension, 6° of lateral flexion, and 2° of rotation, respectively. All boundary conditions were applied to reference points RF1 and RF2 similar to the aforementioned, and the displacements have constrained degrees of freedom except the direction of motion. Displacements were applied to RF1 while RF2 was encastred. The shear strains on the cranial and caudal VEPs were then calculated and visualised in the implicit solver.

Osteoporosis and pycnodysostosis modelling

The OP spine FEM was created in Avizo 3D using 3D erosion in the segmentation module. In the segmentation module, vertebral volume was selected, followed by the application of the built-in selection shrinkage algorithm. A total of 15 times of shrinkage were applied to enlarge the pores and thin the trabecula of the vertebrae. This allows a decreased trabecular volume in the OP vertebrae FEM by ~30%(*35*). After that, the erosive vertebral volume was converted into surface data with a simplified minimum edge length of 32.5 μm. The tetrahedral grids were then created based on the surface data and exported as INP files. The vertebrae INP file was imported into Abaqus CAE to replace the original parts, and the elastic modulus decreased by 67% (3.96 GPa for cortical bone and 49.5 MPa for cancellous bone) in the vertebrae and decreased by 33% (45.5 MPa) in the VEPs(*35*). Regarding the PYCD spine FEM, the model was unchanged but updated with the elastic modulus for the vertebrae and

VEP parts. Due to a lack of experimental data, a conservative estimation of the increase in the elastic modulus by 50% in the PYCD vertebrae (18.0 GPa for cortical bone and 225.0 MPa for cancellous bone) and by 30% in the VEPs (88.3 MPa) was applied, according to the reported increase in the apparent maximum load to failure of 50% in the zebrafish PYCD vertebrae(*34*) and increase in the BMD, which shows a nonlinear positive relationship with the elastic modulus(*37, 38*) in the human PYCD. Simulation of uniaxial compression was performed in Abaqus by applying boundary condition of 3 N concentrated force (along Z direction with constrained zero force at X and Y directions) at RF1 while RF2 was encastred. The force applied is equivalent to 100% body weight of a rat. Model integration, interactions, job analyses, and visualisation were performed as described above. The first principal stress, first principal strain, and third principal strain were obtained for statistical and visual analyses.

Statistical analysis

All the statistical analyses were conducted using SPSS Statistics, and the data were plotted using Origin. The normality and homogeneity of the variance of all of the data were checked, and an independent-samples t test was conducted to compare groups. P values less than 0.05 were considered to indicate statistical significance; $^{*}P < 0.05$, $^{**}P < 0.01$ and $^{***}P < 0.001$. To investigate the agreement between the FEM predictions and DVC measurements, a Bland–Altman plot was generated and described above. To investigate the agreement between the FEM and DVC subvolumes, linear regression was conducted using the average first principal strain at nodes in the FEM subvolumes as the independent variable and that of the DVC subvolumes as the dependent variable. Model fit was assessed using R^2.

Acknowledgements
We gratefully acknowledge Beamtime SM29784 at Diamond Light Source, Beamline I13-2. The authors gratefully acknowledge Joseph Brunet's beneficial comments on the modelling.

Funding: This work was supported by grants EP/V011235/1 and EP/V011006/1 from the UK-Engineering and Physical Sciences Research Council, MR/V033506/1 from the UK-Medical Research Council, grant CZIF2021-006424 from the Chan Zuckerberg Initiative Foundation, and grant 2022-316777 from the Chan Zuckerberg Initiative DAF, an advised fund of Silicon Valley Community Foundation.

Author contributions: Conception and design of the study: P.D.L. and H.S.G. Acquisition of data: J.C., A.P., A.S., E.N., S.M., and A.A.P. Interpretation of data, revision of the manuscript, final approval and agreement to be accountable for all aspects of the work: all authors.
Drafting of the manuscript: J.C., A.P., A.S., and P.D.L.

Competing interests: The authors declare no competing interests.

Data and materials availability: The full sCT scan data are available from the Diamond Light Source data repository under experiment SM29784-6 at beamline I13-2, or from the UCL Research Data Repository (DOI: 10.5522/04/26789212.v1). The full codes are available on Zenodo (DOI: 10.5281/zenodo.13347998).

Supplementary Materials

Supplementary Figures, Supplementary Tables, and Supplementary References.

REFERENCES AND NOTES

1. J. Hartvigsen, M. J. Hancock, A. Kongsted, Q. Louw, M. L. Ferreira, S. Genevay, D. Hoy, J. Karppinen, G. Pransky, J. Sieper, R. J. Smeets, M. Underwood, G. Lancet Low Back Pain Series Working, What low back pain is and why we need to pay attention. *Lancet* **391**, 2356-2367 (2018).
2. G. B. D. Diseases, C. Injuries, Global incidence, prevalence, years lived with disability (YLDs), disability-adjusted life-years (DALYs), and healthy life expectancy (HALE) for 371 diseases and injuries in 204 countries and territories and 811 subnational locations, 1990-2021: a systematic analysis for the Global Burden of Disease Study 2021. *Lancet* **403**, 2133-2161 (2024).
3. G. B. D. L. B. P. Collaborators, Global, regional, and national burden of low back pain, 1990-2020, its attributable risk factors, and projections to 2050: a systematic analysis of the Global Burden of Disease Study 2021. *Lancet Rheumatol* **5**, e316-e329 (2023).
4. A. Qaseem, T. J. Wilt, R. M. McLean, M. A. Forciea, P. Clinical Guidelines Committee of the American College of, T. D. Denberg, M. J. Barry, C. Boyd, R. D. Chow, N. Fitterman, R. P. Harris, L. L. Humphrey, S. Vijan, Noninvasive Treatments for Acute, Subacute, and Chronic Low Back Pain: A Clinical Practice Guideline From the American College of Physicians. *Ann Intern Med* **166**, 514-530 (2017).
5. N. E. Foster, J. R. Anema, D. Cherkin, R. Chou, S. P. Cohen, D. P. Gross, P. H. Ferreira, J. M. Fritz, B. W. Koes, W. Peul, J. A. Turner, C. G. Maher, G. Lancet Low Back Pain Series Working, Prevention and treatment of low back pain: evidence, challenges, and promising directions. *Lancet* **391**, 2368-2383 (2018).
6. J. C. Lotz, A. J. Fields, E. C. Liebenberg, The role of the vertebral end plate in low back pain. *Global Spine J* **3**, 153-164 (2013).
7. Y. Wang, T. Videman, M. C. Battie, ISSLS prize winner: Lumbar vertebral endplate lesions: associations with disc degeneration and back pain history. *Spine (Phila Pa 1976)* **37**, 1490-1496 (2012).
8. Y. Su, D. Ren, Y. Chen, L. Geng, S. Yao, H. Wu, P. Wang, Effect of endplate reduction on endplate healing morphology and intervertebral disc degeneration in patients with thoracolumbar vertebral fracture. *Eur Spine J* **32**, 55-67 (2023).

9. D. J. Hamilton, C. A. Seguin, J. Wang, R. M. Pilliar, R. A. Kandel, T. BioEngineering of Skeletal Tissues, Formation of a nucleus pulposus-cartilage endplate construct in vitro. *Biomaterials* **27**, 397-405 (2006).
10. Y. Hou, Z. Luo, A study on the structural properties of the lumbar endplate: histological structure, the effect of bone density, and spinal level. *Spine (Phila Pa 1976)* **34**, E427-433 (2009).
11. S. A. Rodrigues, K. R. Wade, A. Thambyah, N. D. Broom, Micromechanics of annulus-end plate integration in the intervertebral disc. *Spine J* **12**, 143-150 (2012).
12. K. Madi, K. A. Staines, B. K. Bay, B. Javaheri, H. Geng, A. J. Bodey, S. Cartmell, A. A. Pitsillides, P. D. Lee, In situ characterization of nanoscale strains in loaded whole joints via synchrotron X-ray tomography. *Nat Biomed Eng* **4**, 343-354 (2020).
13. C. M. Disney, K. Madi, A. J. Bodey, P. D. Lee, J. A. Hoyland, M. J. Sherratt, Visualising the 3D microstructure of stained and native intervertebral discs using X-ray microtomography. *Sci Rep* **7**, 16279 (2017).
14. K. A. Staines, K. Madi, B. Javaheri, P. D. Lee, A. A. Pitsillides, A Computed Microtomography Method for Understanding Epiphyseal Growth Plate Fusion. *Front Mater* **4**, 48 (2018).
15. K. A. Staines, K. Madi, S. M. Mirczuk, S. Parker, A. Burleigh, B. Poulet, M. Hopkinson, A. J. Bodey, R. C. Fowkes, C. Farquharson, P. D. Lee, A. A. Pitsillides, Endochondral Growth Defect and Deployment of Transient Chondrocyte Behaviors Underlie Osteoarthritis Onset in a Natural Murine Model. *Arthritis Rheumatol* **68**, 880-891 (2016).
16. C. M. Disney, A. Eckersley, J. C. McConnell, H. Geng, A. J. Bodey, J. A. Hoyland, P. D. Lee, M. J. Sherratt, B. K. Bay, Synchrotron tomography of intervertebral disc deformation quantified by digital volume correlation reveals microstructural influence on strain patterns. *Acta Biomater* **92**, 290-304 (2019).
17. A. Parmenter, C. Disney, F. Bosi, P. D. Lee, Structure and mechanics of the intervertebral disc-endplate junction analysed using synchrotron CT and DVC. *The 28th Congress of the European Society of Biomechanics* **Maastricht, the Netherlands**, (July 9–12, 2023).
18. M. Pena Fernandez, J. Schwiedrzik, A. Burki, F. Peyrin, J. Michler, P. K. Zysset, U. Wolfram, In situ synchrotron radiation microCT indentation of cortical bone: Anisotropic crack propagation, local deformation, and fracture. *Acta Biomater* **167**, 83-99 (2023).
19. C. M. Disney, J. Mo, A. Eckersley, A. J. Bodey, J. A. Hoyland, M. J. Sherratt, A. A. Pitsillides, P. D. Lee, B. K. Bay, Regional variations in discrete collagen fibre mechanics within intact intervertebral disc resolved using synchrotron computed tomography and digital volume correlation. *Acta Biomater* **138**, 361-374 (2022).
20. D. B. Amin, I. M. Lawless, D. Sommerfeld, R. M. Stanley, B. Ding, J. J. Costi, The effect of six degree of freedom loading sequence on the in-vitro compressive properties of human lumbar spine segments. *J Biomech* **49**, 3407-3414 (2016).
21. J. Kusins, N. Knowles, M. Columbus, S. Oliviero, E. Dall'Ara, G. S. Athwal, L. M. Ferreira, The Application of Digital Volume Correlation (DVC) to Evaluate Strain Predictions Generated by Finite Element Models of the Osteoarthritic Humeral Head. *Ann Biomed Eng* **48**, 2859-2869 (2020).

22. P. Stefanek, A. Synek, E. Dall'Ara, D. H. Pahr, Comparison of linear and nonlinear stepwise muFE displacement predictions to digital volume correlation measurements of trabecular bone biopsies. *J Mech Behav Biomed Mater* **138**, 105631 (2023).
23. J. Kusins, N. Knowles, M. Ryan, E. Dall'Ara, L. Ferreira, Full-field comparisons between strains predicted by QCT-derived finite element models of the scapula and experimental strains measured by digital volume correlation. *J Biomech* **113**, 110101 (2020).
24. M. Palanca, S. Oliviero, E. Dall'Ara, MicroFE models of porcine vertebrae with induced bone focal lesions: Validation of predicted displacements with digital volume correlation. *J Mech Behav Biomed Mater* **125**, 104872 (2022).
25. D. Wu, T. Joffre, C. O. Magi, S. J. Ferguson, C. Persson, P. Isaksson, A combined experimental and numerical method to estimate the elastic modulus of single trabeculae. *J Mech Behav Biomed Mater* **125**, 104879 (2022).
26. J. Shen, T. J. Marrow, D. Scotson, X. C. Jin, H. Z. Wu, H. N. A. Chen, Combined evaluation of Young modulus and fracture toughness in small specimens of fine grained nuclear graphite using 3D image analysis. *Journal of Nuclear Materials* **563**, 153642 (2022).
27. J. E. Zorzi, C. A. Perottoni, Estimating Young's modulus and Poisson's ratio by instrumented indentation test. *Materials Science and Engineering a-Structural Materials Properties Microstructure and Processing* **574**, 25-30 (2013).
28. S. Tavana, J. N. Clark, J. Prior, N. Baxan, S. D. Masouros, N. Newell, U. Hansen, Quantifying deformations and strains in human intervertebral discs using Digital Volume Correlation combined with MRI (DVC-MRI). *J Biomech* **102**, 109604 (2020).
29. T. Chai, R. R. Draxler, Root mean square error (RMSE) or mean absolute error (MAE)? - Arguments against avoiding RMSE in the literature. *Geoscientific Model Development* **7**, 1247-1250 (2014).
30. K. Dewitte, C. Fierens, D. Stockl, L. M. Thienpont, Application of the Bland-Altman plot for interpretation of method-comparison studies: a critical investigation of its practice. *Clin Chem* **48**, 799-801; author reply 801-792 (2002).
31. P. S. Myles, J. Cui, Using the Bland-Altman method to measure agreement with repeated measures. *Br J Anaesth* **99**, 309-311 (2007).
32. S. van den Munckhof, A. A. Zadpoor, How accurately can we predict the fracture load of the proximal femur using finite element models? *Clin Biomech (Bristol, Avon)* **29**, 373-380 (2014).
33. L. Hansen, M. de Zee, J. Rasmussen, T. B. Andersen, C. Wong, E. B. Simonsen, Anatomy and biomechanics of the back muscles in the lumbar spine with reference to biomechanical modeling. *Spine (Phila Pa 1976)* **31**, 1888-1899 (2006).
34. E. Kague, F. Turci, E. Newman, Y. Yang, K. R. Brown, M. S. Aglan, G. A. Otaify, S. A. Temtamy, V. L. Ruiz-Perez, S. Cross, C. P. Royall, P. E. Witten, C. L. Hammond, 3D assessment of intervertebral disc degeneration in zebrafish identifies changes in bone density that prime disc disease. *Bone Res* **9**, 39 (2021).
35. J. Wang, B. Zhou, I. Parkinson, C. D. Thomas, J. G. Clement, N. Fazzalari, X. E. Guo, Trabecular Plate Loss and Deteriorating Elastic Modulus of Femoral Trabecular Bone in Intertrochanteric Hip Fractures. *Bone Res* **1**, 346-354 (2013).

36. N. Fratzl-Zelman, A. Valenta, P. Roschger, A. Nader, B. D. Gelb, P. Fratzl, K. Klaushofer, Decreased bone turnover and deterioration of bone structure in two cases of pycnodysostosis. *J Clin Endocrinol Metab* **89**, 1538-1547 (2004).
37. E. A. Abou Neel, A. Aljabo, A. Strange, S. Ibrahim, M. Coathup, A. M. Young, L. Bozec, V. Mudera, Demineralization-remineralization dynamics in teeth and bone. *Int J Nanomedicine* **11**, 4743-4763 (2016).
38. P. Roschger, E. P. Paschalis, P. Fratzl, K. Klaushofer, Bone mineralization density distribution in health and disease. *Bone* **42**, 456-466 (2008).
39. J. Sartori, S. Köhring, S. Bruns, J. Moosmann, J. U. Hammel, Gaining Insight into the Deformation of Achilles Tendon Entheses in Mice. *Advanced Engineering Materials* **23**, 2100085 (2021).
40. D. Christen, A. Levchuk, S. Schori, P. Schneider, S. K. Boyd, R. Muller, Deformable image registration and 3D strain mapping for the quantitative assessment of cortical bone microdamage. *J Mech Behav Biomed Mater* **8**, 184-193 (2012).
41. C. M. Disney, N. T. Vo, A. J. Bodey, B. K. Bay, P. D. Lee, Image quality and scan time optimisation for in situ phase contrast x-ray tomography of the intervertebral disc. *J Mech Behav Biomed Mater* **138**, 105579 (2023).
42. S. Le Cann, E. Tudisco, M. Tagil, S. A. Hall, H. Isaksson, Bone Damage Evolution Around Integrated Metal Screws Using X-Ray Tomography - in situ Pullout and Digital Volume Correlation. *Front Bioeng Biotechnol* **8**, 934 (2020).
43. M. Pena Fernandez, A. P. Kao, R. Bonithon, D. Howells, A. J. Bodey, K. Wanelik, F. Witte, R. Johnston, H. Arora, G. Tozzi, Time-resolved in situ synchrotron-microCT: 4D deformation of bone and bone analogues using digital volume correlation. *Acta Biomater* **131**, 424-439 (2021).
44. M. Palanca, A. J. Bodey, M. Giorgi, M. Viceconti, D. Lacroix, L. Cristofolini, E. Dall'Ara, SYNCHROTRON RADIATION FOR MICROTOMOGRAPHY IMPROVES THE PRECISION OF DIGITAL VOLUME CORRELATION FOR BONE SAMPLES. *Orthopaedic Proceedings* **99-B**, 29-29 (2017).
45. P. J. Thurner, P. Wyss, R. Voide, M. Stauber, M. Stampanoni, U. Sennhauser, R. Muller, Time-lapsed investigation of three-dimensional failure and damage accumulation in trabecular bone using synchrotron light. *Bone* **39**, 289-299 (2006).
46. M. Palanca, A. J. Bodey, M. Giorgi, M. Viceconti, D. Lacroix, L. Cristofolini, E. Dall'Ara, Local displacement and strain uncertainties in different bone types by digital volume correlation of synchrotron microtomograms. *J Biomech* **58**, 27-36 (2017).
47. F. Comini, M. Palanca, L. Cristofolini, E. Dall'Ara, Uncertainties of synchrotron microCT-based digital volume correlation bone strain measurements under simulated deformation. *J Biomech* **86**, 232-237 (2019).
48. H. Dejea, M. Pierantoni, G. A. Orozco, B. W. ET, S. J. Gstohl, C. M. Schleputz, H. Isaksson, In Situ Loading and Time-Resolved Synchrotron-Based Phase Contrast Tomography for the Mechanical Investigation of Connective Knee Tissues: A Proof-of-Concept Study. *Adv Sci (Weinh)* **11**, e2308811 (2024).
49. M. Pena Fernandez, A. H. Barber, G. W. Blunn, G. Tozzi, Optimization of digital volume correlation computation in SR-microCT images of trabecular bone and bone-biomaterial systems. *J Microsc* **272**, 213-228 (2018).
50. M. Pena Fernandez, S. Cipiccia, E. Dall'Ara, A. J. Bodey, R. Parwani, M. Pani, G. W. Blunn, A. H. Barber, G. Tozzi, Effect of SR-microCT radiation on the

mechanical integrity of trabecular bone using in situ mechanical testing and digital volume correlation. *J Mech Behav Biomed Mater* **88**, 109-119 (2018).
51. A. Zwahlen, D. Christen, D. Ruffoni, P. Schneider, W. Schmolz, R. Muller, Inverse finite element modeling for characterization of local elastic properties in image-guided failure assessment of human trabecular bone. *J Biomech Eng* **137**, (2015).
52. M. J. Turunen, S. Le Cann, E. Tudisco, G. Lovric, A. Patera, S. A. Hall, H. Isaksson, Sub-trabecular strain evolution in human trabecular bone. *Sci Rep* **10**, 13788 (2020).
53. L. Yan, A. Cinar, S. Ma, R. Abel, U. Hansen, T. J. Marrow, A method for fracture toughness measurement in trabecular bone using computed tomography, image correlation and finite element methods. *J Mech Behav Biomed Mater* **109**, 103838 (2020).
54. J. Kok, E. Tornquist, D. B. Raina, S. Le Cann, V. Novak, A. Sirka, L. Lidgren, L. Grassi, H. Isaksson, Fracture behavior of a composite of bone and calcium sulfate/hydroxyapatite. *J Mech Behav Biomed Mater* **130**, 105201 (2022).
55. S. Martelli, M. Giorgi, E. Dall' Ara, E. Perilli, Damage tolerance and toughness of elderly human femora. *Acta Biomater* **123**, 167-177 (2021).
56. A. L. Parmenter, E. Newham, A. Sharma, C. M. Disney, H. Deyhle, F. Bosi, N. J. Terrill, B. K. Bay, A. A. Pitsillides, H. S. Gupta, P. D. Lee, Multimodal imaging reveals multiscale mechanical interplay in vertebral endplate microarchitecture during intervertebral disc loading. *bioRxiv*, 2024.2008.2019.608559 (2024).
57. E. Dall'Ara, A. J. Bodey, H. Isaksson, G. Tozzi, A practical guide for in situ mechanical testing of musculoskeletal tissues using synchrotron tomography. *J Mech Behav Biomed Mater* **133**, 105297 (2022).
58. M. Egermann, J. Goldhahn, E. Schneider, Animal models for fracture treatment in osteoporosis. *Osteoporos Int* **16 Suppl 2**, S129-138 (2005).
59. J. Aerssens, S. Boonen, G. Lowet, J. Dequeker, Interspecies differences in bone composition, density, and quality: potential implications for in vivo bone research. *Endocrinology* **139**, 663-670 (1998).
60. D. M. Elliott, J. J. Sarver, Young investigator award winner: validation of the mouse and rat disc as mechanical models of the human lumbar disc. *Spine (Phila Pa 1976)* **29**, 713-722 (2004).
61. A. A. Espinoza Orias, N. R. Malhotra, D. M. Elliott, Rat disc torsional mechanics: effect of lumbar and caudal levels and axial compression load. *Spine J* **9**, 204-209 (2009).
62. A. A. Rao, G. A. Dumas, Influence of material properties on the mechanical behaviour of the L5-S1 intervertebral disc in compression: a nonlinear finite element study. *J Biomed Eng* **13**, 139-151 (1991).
63. M. A. Liebschner, D. L. Kopperdahl, W. S. Rosenberg, T. M. Keaveny, Finite element modeling of the human thoracolumbar spine. *Spine (Phila Pa 1976)* **28**, 559-565 (2003).
64. R. R. Patel, A. Noshchenko, R. Dana Carpenter, T. Baldini, C. P. Frick, V. V. Patel, C. M. Yakacki, Evaluation and Prediction of Human Lumbar Vertebrae Endplate Mechanical Properties Using Indentation and Computed Tomography. *J Biomech Eng* **140**, 1010111-1010119 (2018).
65. J. P. Grant, T. R. Oxland, M. F. Dvorak, Mapping the structural properties of the lumbosacral vertebral endplates. *Spine (Phila Pa 1976)* **26**, 889-896 (2001).

66. B. K. Bay, T. S. Smith, D. P. Fyhrie, M. Saad, Digital volume correlation: Three-dimensional strain mapping using X-ray tomography. *Experimental Mechanics* **39**, 217-226 (1999).
67. F. Gillard, R. Boardman, M. Mavrogordato, D. Hollis, I. Sinclair, F. Pierron, M. Browne, The application of digital volume correlation (DVC) to study the microstructural behaviour of trabecular bone during compression. *J Mech Behav Biomed Mater* **29**, 480-499 (2014).
68. D. L. Kopperdahl, T. M. Keaveny, Yield strain behavior of trabecular bone. *J Biomech* **31**, 601-608 (1998).
69. J. Liu, L. Hao, L. Suyou, Z. Shan, M. Maiwulanjiang, S. Li, C. Wang, S. Fan, F. Zhao, Biomechanical properties of lumbar endplates and their correlation with MRI findings of lumbar degeneration. *J Biomech* **49**, 586-593 (2016).
70. T. G. Lowe, S. Hashim, L. A. Wilson, M. F. O'Brien, D. A. Smith, M. J. Diekmann, J. Trommeter, A biomechanical study of regional endplate strength and cage morphology as it relates to structural interbody support. *Spine (Phila Pa 1976)* **29**, 2389-2394 (2004).
71. N. M. Grosland, V. K. Goel, Vertebral endplate morphology follows bone remodeling principles. *Spine (Phila Pa 1976)* **32**, E667-673 (2007).
72. B. Javaheri, H. Razi, S. Gohin, S. Wylie, Y. M. Chang, P. Salmon, P. D. Lee, A. A. Pitsillides, Lasting organ-level bone mechanoadaptation is unrelated to local strain. *Sci Adv* **6**, eaax8301 (2020).
73. Y. Cao, S. Liao, H. Zeng, S. Ni, F. Tintani, Y. Hao, L. Wang, T. Wu, H. Lu, C. Duan, J. Hu, 3D characterization of morphological changes in the intervertebral disc and endplate during aging: A propagation phase contrast synchrotron micro-tomography study. *Sci Rep* **7**, 43094 (2017).
74. T. Maruyama, T. Nakamae, N. Kamei, T. Morisako, K. Nakao, F. Farid, H. Fukui, N. Adachi, Development of a novel animal model of lumbar vertebral endplate lesion by intervertebral disk injection of monosodium iodoacetate in rats. *Eur Spine J* **33**, 2116-2128 (2024).
75. Y. Wang, T. Videman, M. C. Battie, Morphometrics and lesions of vertebral end plates are associated with lumbar disc degeneration: evidence from cadaveric spines. *J Bone Joint Surg Am* **95**, e26 (2013).
76. W. Li, H. Zhao, S. Zhou, Z. Xiong, W. Zhong, J. Guan, T. Liu, Y. Yang, X. Yu, Does vertebral osteoporosis delay or accelerate lumbar disc degeneration? A systematic review. *Osteoporos Int* **34**, 1983-2002 (2023).
77. A. J. Walsh, J. C. Lotz, Biological response of the intervertebral disc to dynamic loading. *J Biomech* **37**, 329-337 (2004).
78. Y. Zhang, B. A. Lenart, J. K. Lee, D. Chen, P. Shi, J. Ren, C. Muehleman, D. Chen, H. S. An, Histological features of endplates of the mammalian spine: from mice to men. *Spine (Phila Pa 1976)* **39**, E312-317 (2014).
79. A. Parmenter, E. Newham, A. Sharma, C. Disney, H. Deyhle, F. Bosi, N. J. Terrill, B. Bay, A. A. Pitsillides, H. Gupta, P. Lee. (University College London, 2024).